Three-Dimensional Printed Ultrabroadband Terahertz Metamaterial Absorbers

Zhonglei Shen,[1,2,3,‡] Shengnan Li,[1,‡] Yafei Xu,[1] Wei Yin,[1] Liuyang Zhang,[1,2,3,*] and
Xuefeng Chen[1,†]

[1] *State Key Laboratory for Manufacturing Systems Engineering, Xi'an Jiaotong University, Xi'an, Shanxi, 710049, People's Republic of China*
[2] *Zhejiang Research Institute of Xi'an Jiaotong University, Hangzhou, Zhejiang, 311215, People's Republic of China*
[3] *Xi'an Jiaotong University Shenzhen Academy, Nanshan District, Science and Technology Park, Shenzhen, 518057, People's Republic of China*

(Received 9 May 2021; revised 2 July 2021; accepted 6 July 2021; published 28 July 2021)

Terahertz (THz) absorbers have recently attracted extensive attention for their promising potential in various applications; however, many existing THz absorbers are restrained by their narrow bandwidth and complicated and costly fabrication process that renders them unfavorable for practical devices. Herein, we propose a stereoscopic multilayered ultrabroadband THz metamaterial absorber by stacking multilayer concentric resonators on different-level top surfaces of a monolithic three-dimensional (3D) pagodalike substrate. By taking full advantage of the 3D printing technique, the proposed ultrabroadband absorber can be produced efficiently in an easy three-step process that overcomes the fabrication complexities of traditional multistep photolithography processes. Additionally, the feasibility and robustness of the proposed fabrication method for common out-of-plane THz narrowband absorbers are also validated, and the absorption capacities of the 3D printed absorbers are numerically and experimentally elucidated. These results might provide an efficient concept and fabrication technique to stimulate many potential applications in emerging THz technologies, such as sensing, imaging, and wireless communications.

DOI: 10.1103/PhysRevApplied.16.014066

I. INTRODUCTION

Metamaterials, consisting of artificially constructed electromagnetic materials, have attracted considerable research interest in the past decade, owing to their capabilities of providing an innovative approach to manipulate electromagnetic responses in sensing, imaging, and wireless communications [1–6]. Recently, terahertz (THz) metamaterials with an out-of-plane morphology design have been widely proposed for various promising applications, including narrowband absorbers [7,8], optical antireflection [9,10], modulators [11], and polarization convertors [12]. Among them, the THz narrowband absorbers demonstrate enhanced sensing sensitivity for analytes, as the out-of-plane morphology can ameliorate spatial overlap and interactions between the analyte and the localized hot spots [7]. Conventionally, out-of-plane THz narrowband absorbers are fabricated by standard photolithography techniques, which normally require complicate procedures and relatively high cost. Thus, a simple, low-cost, and lithography-free fabrication method for THz narrowband-absorber-based highly sensitive sensors will be beneficial for the prosperous development of THz devices.

In addition, THz broadband metamaterial absorbers are also highly desirable in various applications [13–18]. However, the broadband absorption remains a huge challenge due to the intrinsically narrow bandwidth of surface-plasmon polaritons and localized surface-plasmon resonances on the nanoscale metallic surface [19]. Thus, great efforts are devoted to expanding the bandwidth of metamaterial absorbers. The most efficient approach is to laterally [20–22] or longitudinally [23–25] superimpose multiple resonators with different sizes in one unit cell. However, the bandwidth of the former might be limited to the fact that the unit cell must be smaller than the wavelength for the metamaterial absorber [16], while the latter has attractive potential to expand the bandwidth, as it provides additional freedom in stacking the resonant units along the vertical direction and eventually to produce a stereoscopic multilayered THz metamaterial broadband absorber [26–31]. However, the fabrication of multilayered absorbers inevitably involves sophisticated multistep photolithography processes that are time-consuming and too complicated to be extensively implemented in

---

[*] liuyangzhang@xjtu.edu.cn
[†] chenxf@xjtu.edu.cn
[‡] Z. Shen and S. Li contributed equally to this work.

practical applications. Thus, it also remains formidable challenge to fabricate a stereoscopic multilayered THz metamaterial absorber with ultrabroad bandwidth through a simple, low-cost, lithography-free, and high-throughput strategy.

Herein, we propose a polarization-independent ultrabroadband THz metamaterial absorber via a simple fabrication method. The ultrabroadband absorber consists of stacking multilayered concentric ring resonators on different-level top surfaces of the monolithic three-dimensional (3D) printed pagodalike substrate. The ultrabroad absorption bandwidth is achieved by the overlap of multiple resonant modes from the concentric rings between adjacent layers. Different from previous stereoscopic multilayered broadband THz metamaterial absorbers prepared via multistep photolithography processes, the ultrabroadband absorber is realized through a simple three-step fabrication process. In addition, to demonstrate the robustness of the proposed fabrication method, conventional THz narrowband absorbers are also experimentally validated. These findings can provide an efficient concept and efficient fabrication solution for THz absorbers with favorable bands and shed light on various types of functional devices available through the high-throughput fabrication technique.

II. CONCEPT AND METAMOLECULE DESIGN

Figure 1(a) is a schematic diagram of the unit cell (metamolecule) of the proposed stereoscopic multilayered THz absorber. The absorber consists of a top gold-disk resonator (meta-atom I) and multiple-layer gold concentric ring resonators with gradient geometric parameters (meta-atom II) stacked vertically on different-level top surfaces of the monolithic 3D pagodalike resin substrate without overlapping each other. An underlaid gold back-reflector is employed to prohibit transmission of the incident terahertz wave. Meta-atom I and II based out-of-plane THz absorbers I and II, shown in Figs. 1(b) and 1(c), are also modeled for comparison purposes. To investigate the absorption properties of the proposed absorbers, all full-wave numerical simulations are performed by using CST Microwave Studio software (see Appendix A for more details). The conductivity of gold is set a $4.561 \times 10^{7}\ \mathrm{S\,m^{-1}}$ and the relative permittivity and loss tangent of the resin substrate are $\varepsilon = 2.8$ and $\tan\delta = 0.08$ at 1 THz, respectively; these values are extracted from data measured by THz time-domain spectroscopy (THz TDS) (see Appendix B for more details). The absorption, $A(\omega)$, is calculated by $A(\omega) = 1 - R(\omega) - T(\omega)$, where $R(\omega)$ represents the reflection and $T(\omega)$ represents the transmission.

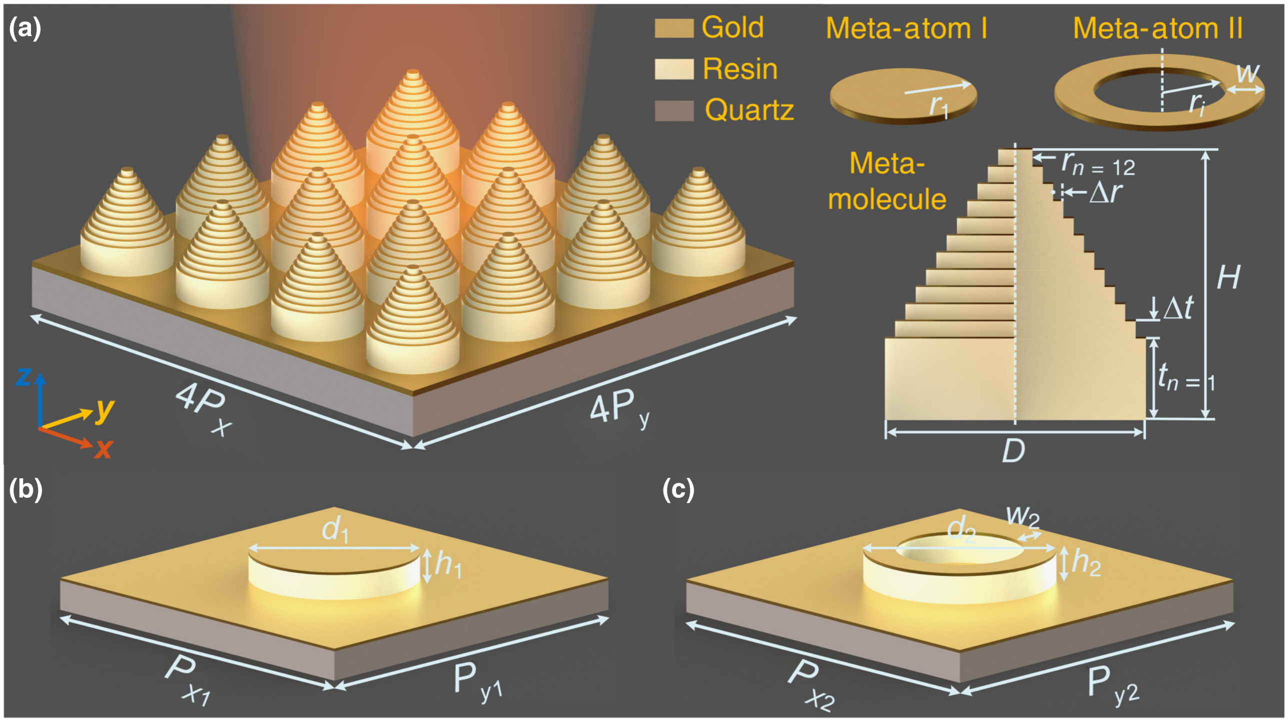

FIG. 1. (a) Schematic diagram of stereoscopic multilayered THz absorber, where $P_x = P_y = 77\ \mu$m, $t_1 = 17\ \mu$m, $\Delta t = 2\ \mu$m, $r_{12} = 10\ \mu$m, $\Delta r = w = 2\ \mu$m, $H = 39.2\ \mu$m, and $D = 50\ \mu$m. (b) Meta-atom I based THz absorber I, where $P_{x1} = P_{y1} = 270\ \mu$m, $d_1 = 114\ \mu$m, and $h_1 = 20\ \mu$m. (c) Meta-atom II based THz absorber II, where $P_{x2} = P_{y2} = 240\ \mu$m, $d_2 = 116\ \mu$m, $w_2 = 16\ \mu$m, and $h_2 = 20\ \mu$m.

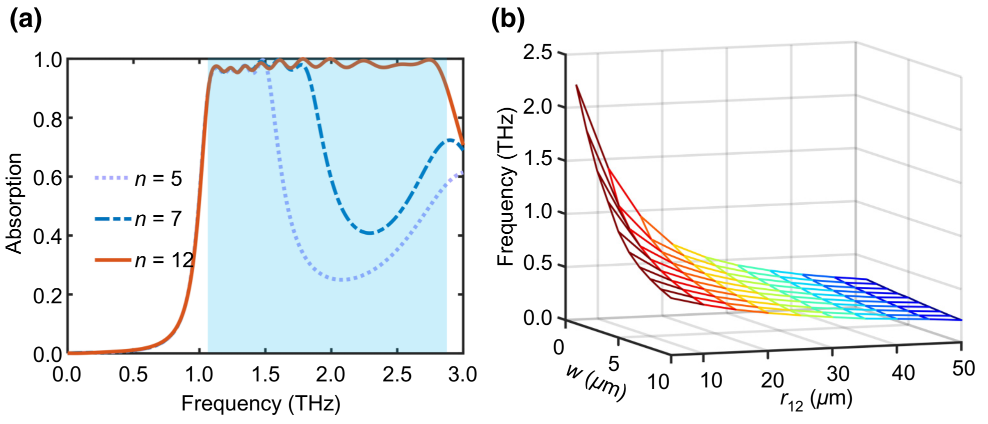

FIG. 2. (a) Absorption spectra of THz ultrabroadband absorber with various stacked layers (n). (b) Initial resonant frequency as a function of radius, r_{12}, of meta-atom I and width, w, of meta-atom II.

Here, $T(\omega)$ is always equal to zero, as the thickness of ground gold reflector is much larger than the skin depth of the incident THz wave.

III. RESULTS AND DISCUSSION

Figure 2(a) depicts the absorption spectra of proposed absorbers with various stacked layers [Fig. 1(a)] at normal incidence. It is clearly observed that the absorbers achieve near-unity absorption spectra with significantly increased bandwidths (defined as absorption ≥ 90% in this work) when the vertically stacked layers (n) of meta-atoms I and II increase from 5 to 12. Specifically, the absorption bandwidth of the absorbers with $n = 12$ is up to 1.81 THz (from 1.07 to 2.88 THz), which explicitly implies that the absorber possesses an ultrabroadband near-unity absorption property. Apparently, the absorption bandwidth of the ultrabroadband absorber can be flexibly controlled by elaborately engineering the stacked layers of meta-atoms II, and the increment of the out-of-plane stacking layer

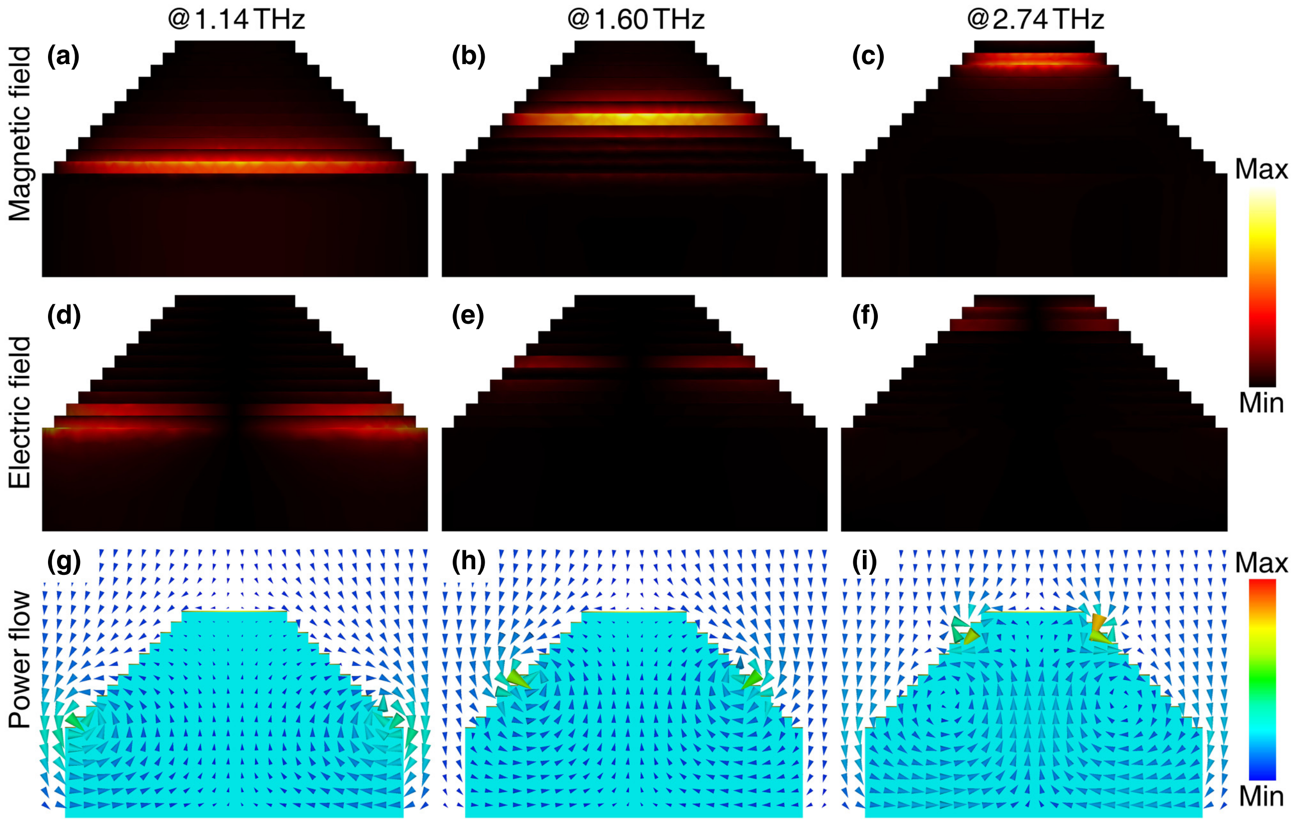

FIG. 3. Magnetic field distributions of ultrabroadband absorber at (a) 1.14 THz, (b) 1.60 THz, and (c) 2.74 THz. Electric field distributions of ultrabroadband absorber at (d) 1.14 THz, (e) 1.60 THz, and (f) 2.74 THz. Power-flow distributions of ultrabroadband absorber at (g) 1.14 THz, (h) 1.60 THz, and (i) 2.74 THz.

from the experimental viewpoint is trivial for our proposed fabrication method. Additionally, changes to geometric parameters r_{12} and w of meta-atoms I and II can also tune the initial resonant frequency [Fig. 2(b)] and absorption bandwidth (see Appendix C for more details) of the proposed ultrabroadband absorber. In the following sections, unless otherwise stated, the ultrabroadband absorber with $n = 12$ is chosen as an example to further analyze its fundamental mechanism of bandwidth expansion.

To further elucidate the bandwidth-expansion mechanism of the broadband absorber, the magnetic field, electric field, and power-flow distributions at specific resonant frequencies (1.14, 1.60, and 2.74 THz) are depicted in Fig. 3. From Figs. 3(a)–3(c), it is found that the induced magnetic field localized at the center of the 3D pagodalike structure originates from the antiparallel surface current at two neighboring concentric ring structures and eventually generates a magnetic resonance between adjacent resonators (see Appendix D for more details). The induced electric field localized on the sides of the pagodalike structure is induced by accumulated charges on the concentric ring structure, as shown in Figs. 3(d)–3(f). In Figs. 3(g)–3(i), the power flow encircles the accumulated charges to generate energy vortexes along the sidewall of the pagodalike structure. When the energy vortexes pass the sidewall of the pagodalike structure repeatedly, most of the incident-wave energy will be dissipated spontaneously and near-unity absorption can be achieved. Furthermore, it is worth noting that the THz wave at high frequencies is absorbed at the upper parts of the ultrabroadband absorber, while those of lower frequencies are absorbed at the lower parts. Ultrabroadband absorption spectra are obtained by the overlap of multiple resonant modes from the concentric rings between adjacent layers.

Additionally, a broadband absorber with a high absorption efficiency for oblique incidence is highly sought-after for practical applications. Figure 4 depicts the absorption spectra of the ultrabroadband absorber at various incident angles from TE and TM polarizations. From Figs. 4(a) and 4(b), absorption is polarization insensitive for THz waves under the normal incidence due to the structural symmetry of the pagodalike structure, and the broadband absorption performance for both TE and TM polarizations exhibit trivial changes when the incident angle, θ, is below 30°. When the incident angle goes beyond 30°, the absorption spectra are gradually

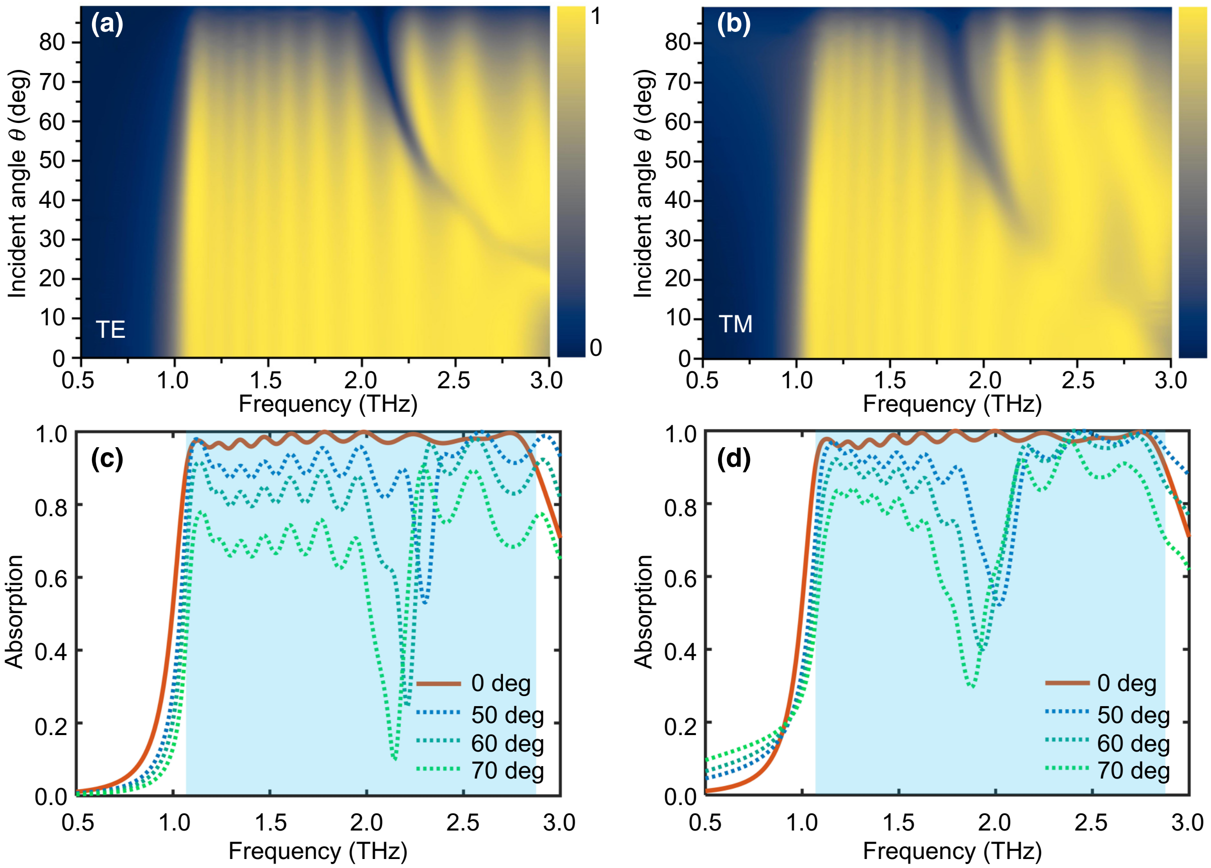

FIG. 4. Dependence of absorption spectra of ultrabroadband absorber on incident angle θ for (a) TE and (b) TM polarizations. The absorption spectra at specified incident angles for (c) TE and (d) TM polarizations.

degraded and split into two independent broadband absorption peaks as θ increases from about 30° to 88°. The peak at high frequencies has a higher absorptance than that at low frequencies, which might be attributed to high-order resonant modes excited by the 3D structure at high frequencies. In Figs. 4(c) and 4(d), the absorption performance of the ultrabroadband absorber is more sensitive for the TE wave than that of the TM wave with the variation of θ, as the absorption spectra originate from the overlap of multiple magnetic resonances. For TE-wave incidence, the magnetic component gradually decreases with the increment of θ, while the magnetic component under TM incidence retains a constant value. In this circumstance, the magnetic resonances can be effectively excited, and thus, the ultrabroadband absorption spectra are more sensitive for the TE wave than that for the TM wave as θ varies. In brief, the proposed ultrabroadband terahertz absorber is angle insensitive and polarization insensitive, and thus, is promising for practical applications.

To experimentally demonstrate the absorption performance of the proposed THz absorbers, the absorber is fabricated through an easy 3D printing technique and characterized by the THz TDS system. Figure 5(a) shows a schematic representation of the simple three-step fabrication process for the ultrabroadband absorber. First, electron-beam (EB) deposition is employed to successively deposit 10-nm-thick Cr and 200-nm-thick Au on the clean quartz substrate, in which the Cr layer functions as an adhesion layer to enhance adhesion between the quartz substrate and the metallic Au layer. Next, the 3D pagodalike resin microstructures are layer-by-layer printed on the Cr/Au layer as the out-of-plane dielectric substrate of the ultrabroadband absorber by using a projection microstereolithography-based 3D printing technique (BMF Nano Materials Technology Co., Ltd). The dielectric substrate prebuilt with the mapping software is sliced into a sequence of two-dimensional mask images with predetermined layer thicknesses followed by an exposure process. By iterating this printing step for each layer,

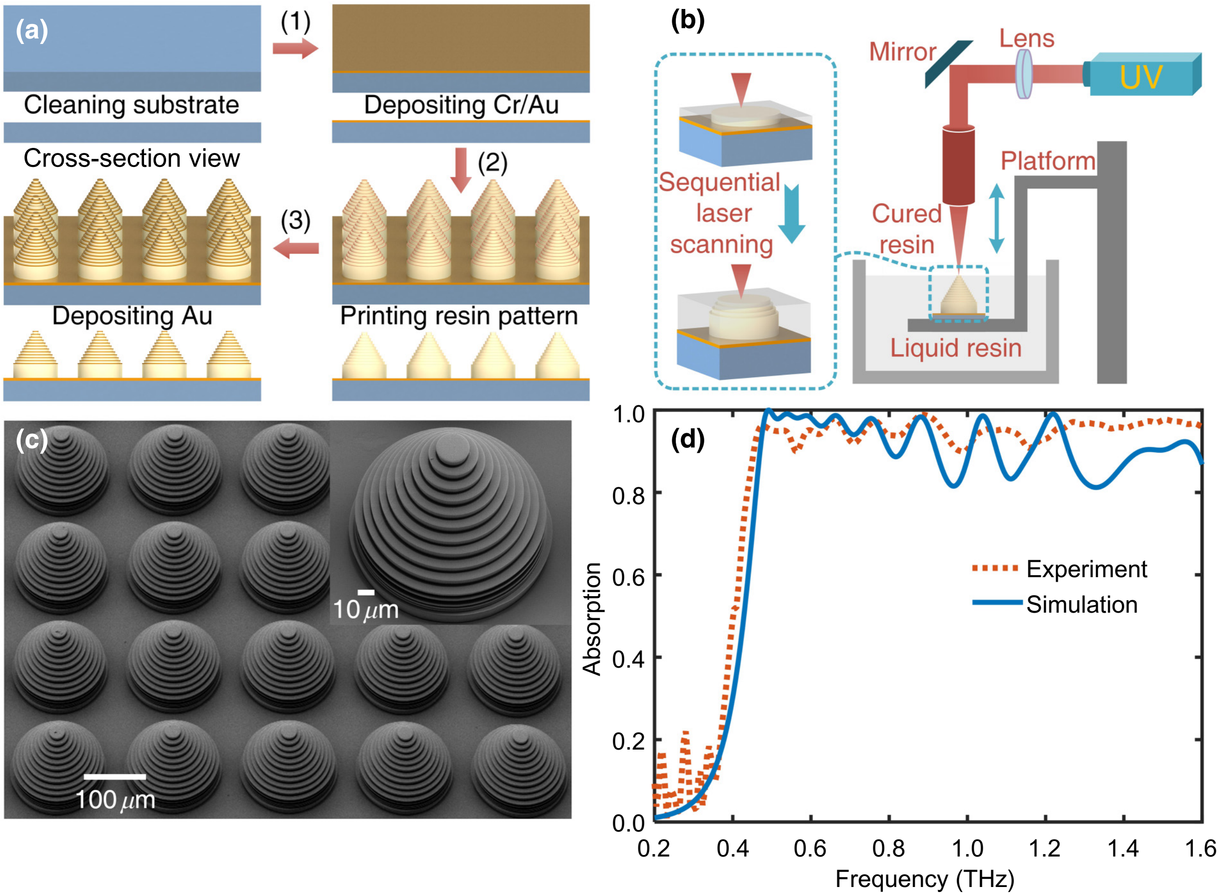

FIG. 5. (a) Fabrication process for ultrabroadband THz absorber. (b) Schematic diagram of projection microstereolithography-based 3D printing technique. (c) SEM image of fabricated ultrabroadband THz absorber, where $P_x = P_y = 185$ μm, $r_{12} = 10$ μm, $\Delta r = w = 6$ μm, $t_1 = 50$ μm, and $\Delta t = 10$ μm. (d) Experimental and simulated absorption spectra of ultrabroadband THz absorber.

the entire dielectric substrate will be created [Fig. 5(b)]. Finally, on the different-level top surfaces of the printed out-of-plane dielectric substrate, a 200-nm-thick Au layer is then deposited by EB deposition. A stereoscopic multilayered ultrabroadband THz absorber is fabricated by the simple three-step fabrication process.

The stereoscopic multilayered ultrabroadband THz absorber with easily implementable geometric parameters [in Fig. 5(c)] is fabricated as a proof-of-prototype by introducing this facile fabrication strategy. Figure 5(c) shows the oblique scanning electron microscopy (SEM) images of the fabricated stereoscopic multilayered ultrabroadband absorber. The outline of the stacked multilayer concentric ring is neat, except for the radius of the bottom-layer ring-shaped resonator being slightly larger than that of the adjacent top layer; this is attributed to the overcuring effect during the 3D printing process to enhance adhesion between the 3D pagodalike resin and the Cr/Au layer. Figure 5(d) depicts the absorption spectra measured by using THz TDS (see Appendix A for more details) and simulated absorption spectra of the fabricated ultrabroadband absorber. It can be seen that the absorber has an absorption bandwidth of 1.19 THz (from 0.41 to 1.60 THz); the measured initial resonant frequency agrees well with that from the simulation; and the slightly higher absorptivity from the measurement than that of the simulation can be ascribed to fabrication errors, as well as an underestimated reflectivity because the full-angle scattering effect of incident waves is enhanced, as the wavelength is closer to the size of the metamolecule at high frequencies and some of the scattered waves are not collected in the reflectivity due to experimental limitations.

Finally, the two THz narrowband absorbers in Figs. 1(b) and 1(c) are also fabricated and shown in Figs. 6(a) and 6(b) to demonstrate the robustness of the proposed fabrication process for traditional photolithography-based THz devices. Figures 6(c) and 6(d) show the measured and simulated absorption spectra of absorbers I and II at normal incidence, respectively. It is worth noting that the resonant frequencies of the measured absorption spectra of both absorbers I and II agree well with the simulated results, while the absorption bandwidth of the measured

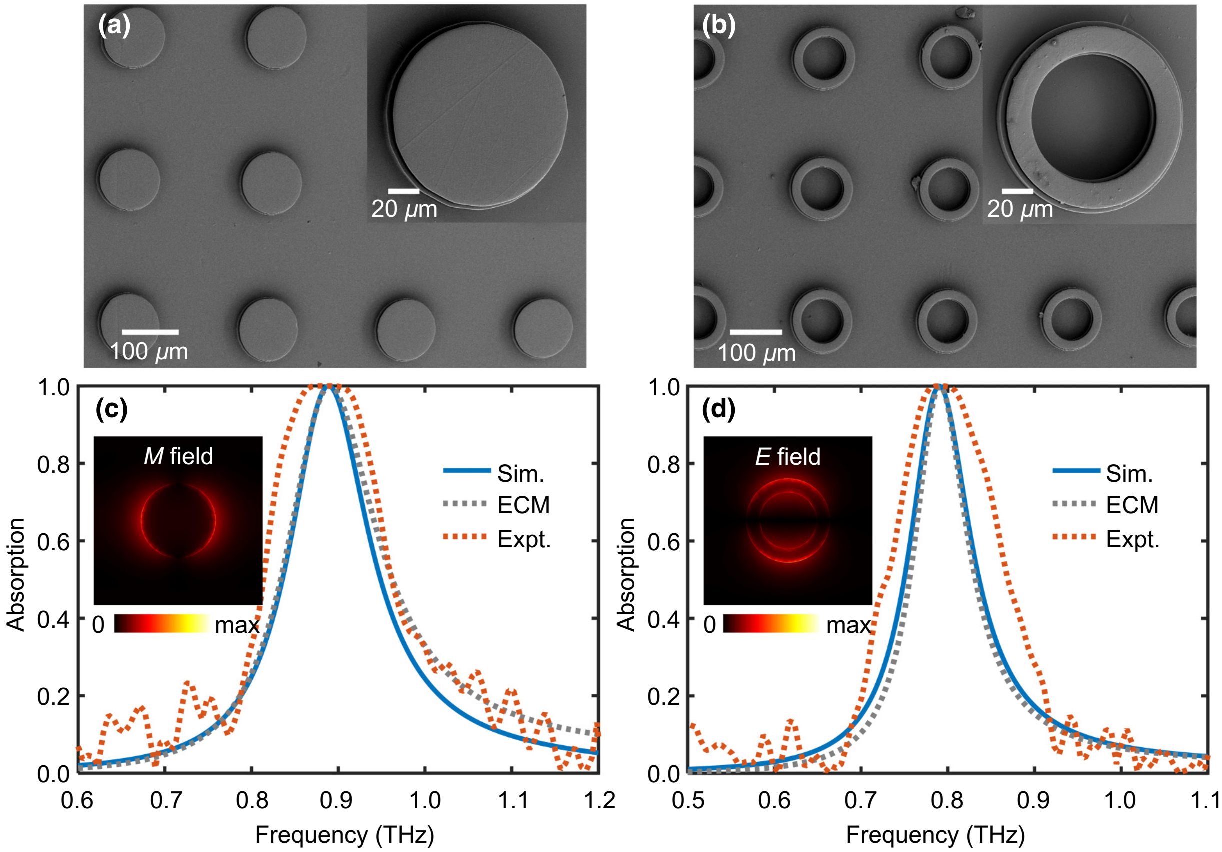

FIG. 6. SEM images of fabricated (a) meta-atom I based THz narrowband absorber I and (b) meta-atom II based narrowband absorber II; geometric parameters are given in captions of Figs. 1(b) and 1(c). Simulated, theoretical, and experimental absorption spectra of fabricated (c) THz narrowband absorber I, inset shows top view of the magnetic field distribution at 0.89 THz, and (d) THz narrowband absorber II, inset shows top view of the electric field distribution at 0.79 THz.

results is broader than that from the simulation, which might be attributed to the large damping (loss) in the Au layers of the fabricated absorbers, as the conductivity of Au films is smaller than that of the bulk counterparts in the simulations [32]. The near-unity absorption spectra of narrowband absorbers I and II can be attributed to the excitation of a magnetic dipole resonance at 0.89 THz [inset of Fig. 6(c)] and the excitation of an electric dipole resonance at 0.79 THz [inset of Fig. 6(d)], respectively. Additionally, an analytical equivalent circuit model (ECM) (see Appendix E for more details) is also utilized to explain the narrowband electromagnetic response of two absorbers. Detailed parameters of the ECM model are provided in Appendix E. From Figs. 6(c) and 6(d), it can be observed that the absorption spectra from the analytical ECM agree well with those measured and the simulated results in the frequency region of interest. As a consequence, the presented fabrication process is capable of providing a simple, low-cost, and high-quality fabrication solution for both out-of-plane narrowband and stereoscopic multilayered ultrabroadband THz absorbers; this holds great promise for the development of metamaterial-absorber-based THz devices, such as spatial light modulators [11] and high-sensitivity sensors [7,8].

IV. CONCLUSIONS

We experimentally demonstrate a polarization-independent ultrabroadband THz metamaterial absorber that consists of stacking multilayer concentric resonators on different-level top surfaces of a monolithic 3D pagoda-like substrate, to overcome the manufacturing difficulties for preparing stereoscopic multilayered ultrabroadband THz absorbers and common narrowband THz absorbers through a simple low-cost 3D-printing-based fabrication process. The fabricated ultrabroadband absorber exhibits high absorptivity within an ultrabroad bandwidth ranging from 0.41 to 1.60 THz. This work might stimulate many potential applications in THz sensing, imaging, and wireless communications.

ACKNOWLEDGMENTS

This work is supported by the National Natural Science Foundation of China (51805414), the Zhejiang Provincial Natural Science Foundation of China (LZ19A020002), and the Science and Technology Innovation Committee of Shenzhen Municipality (JCYJ20180306170652664) to L.Z.

APPENDIX A: NUMERICAL SIMULATIONS AND EXPERIMENTAL SETUP

The full-wave numerical simulations are performed by using the frequency-domain solver of the commercial finite-element software package CST Microwave Studio. In the simulations, the unit-cell boundary conditions are used in the x and y directions to simulate the periodic array, and open boundary conditions are employed along the propagation direction to avoid multiple reflections. The mesh size meets the requirements for convergence and accuracy, and the unit cells are illuminated with normally incident linear plane waves, unless otherwise specified.

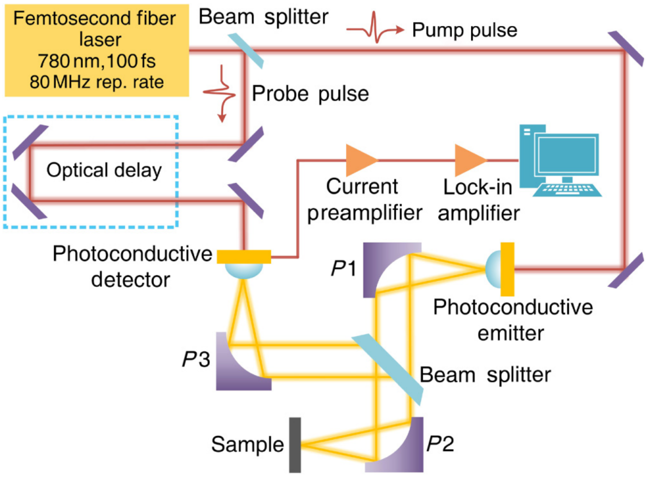

FIG. 7 Schematic diagram of experimental setup.

All reflection spectra of the fabricated absorbers are measured by using a commercial THz TDS system based on photoconductive antennas (TERAPULSE LX-K, TERAVIEW Co., Ltd), as shown in Fig. 7. This system has a frequency bandwidth in the range of 0.06–4 THz with a spectral resolution of 5 GHz. In the THz TDS system, a femtosecond fiber laser with a pulse width of 100 fs and 80 MHz reception rate are adopted to illuminate a biased photoconductive emitter to generate terahertz pulses. The THz pulses are focused on the absorbers by a pair of parabolic mirrors (*P*1 and *P*2), and the reflected waves are collected by *P*2 with a numerical aperture of 0.36 and focused by *P*3 onto a photoconductive detector to record the time-domain response. The measured signals are converted from time-domain data to frequency-domain data through fast Fourier transform. A reference measurement of the reflectance is first performed on the standard gold mirror, and the raw reflectance measurements are then performed on the fabricated absorbers and normalized to the reference measurement to exclude environmental absorption. All measurements are carried out in dry air at 30 °C to reduce undesired THz absorption by water vapor.

APPENDIX B: DIELECTRIC PROPERTIES OF RESIN SUBSTRATE

To obtain the complex relative permittivity $\varepsilon(\omega) = \varepsilon'(\omega) - j\varepsilon''(\omega)$ and loss tangent $\tan(\delta)$ of resin substrate, the resin substrate is characterized by a transmission-type THz

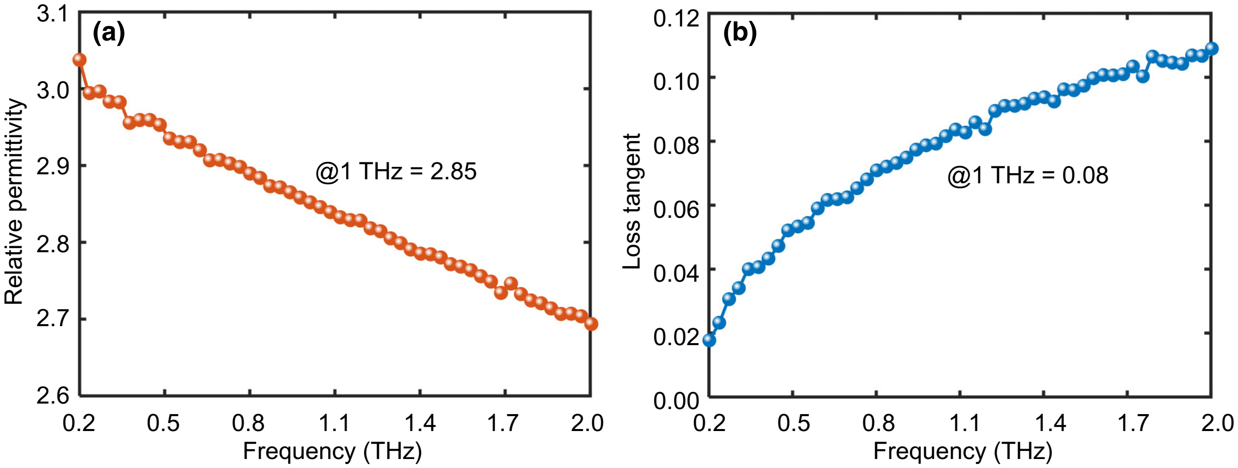

FIG. 8 Measured (a) relative permittivity and (b) loss tangents of resin substrate.

TDS. Figures 8(a) and 8(b) depict the measured relative permittivity and loss tangent of resin substrate, respectively, where the real and the imaginary parts of relative permittivity can be calculated by

$$\varepsilon'(\omega) = (n_r(\omega))^2 - \left(\frac{c_0\gamma(\omega)}{2\omega}\right)^2 \tag{B1}$$

$$\varepsilon''(\omega) = \frac{c_0 n_r(\omega)\gamma(\omega)}{\omega} \tag{B2}$$

where ω is the annular frequency of incident waves, c_0 is the light velocity in vacuum, $n_r(\omega)$ and $\gamma(\omega)$ are the refractive index and the absorption coefficient of resin substrate, respectively, which can be expressed as

$$n_r(\omega) = \varphi(\omega)\frac{c_0}{d} + 1 \tag{B3}$$

$$\gamma(\omega) = \frac{2}{d}\ln\left(\frac{4n_r(\omega)}{\rho(\omega)(n_r(\omega)+1)^2}\right) \tag{B4}$$

where $\rho(\omega)$ and $\alpha(\omega)$ are the amplitude and the phase of the ratio of transmitted frequency domain signals with and without resin substrate. Finally, the loss tangent of resin substrate can be computed by $\tan\delta = \varepsilon''/\varepsilon'$.

APPENDIX C: ABSORPTION SPECTRA OF THE ULTRABROADBAND THZ ABSORBER WITH RESPECT TO GEOMETRIC PARAMETERS

From Figs. 9(a) and 9(b), it's clearly observed that a distinct redshift of the initial resonant frequency of proposed ultrabroadband absorber appears when r_{12} increases from 5 to 15 or w increases from 1 to 3 and the absorption bandwidth of ultrabroadband absorber can also be controlled through changing geometric parameters r_{12} and w, respectively, indicating that the operating frequencies and the

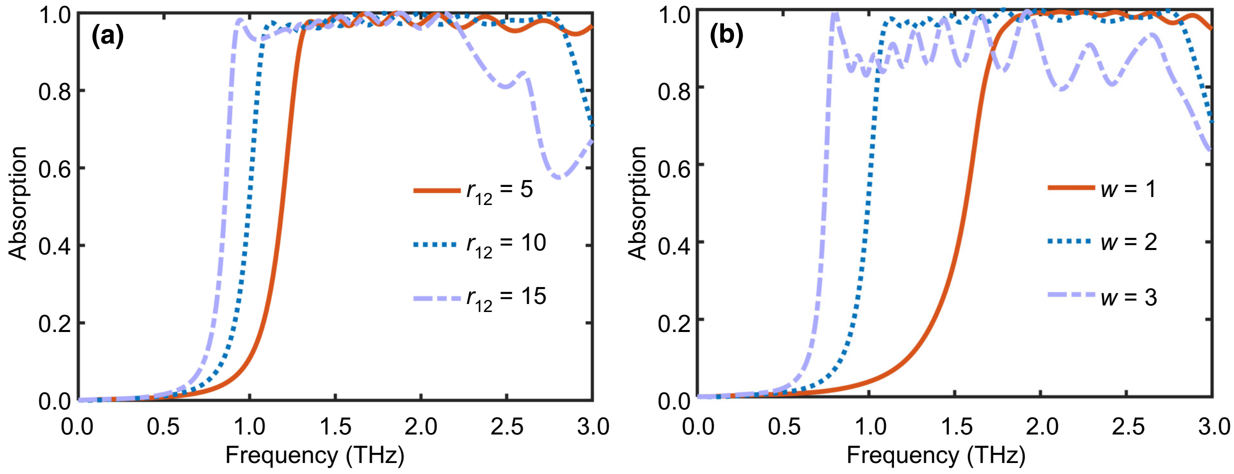

FIG. 9 (a) Absorption spectra of ultrabroadband THz absorber with respect to radius, r_{12}, of meta-atom I. (c) Absorption spectra with respect to width, w, of meta-atom II.

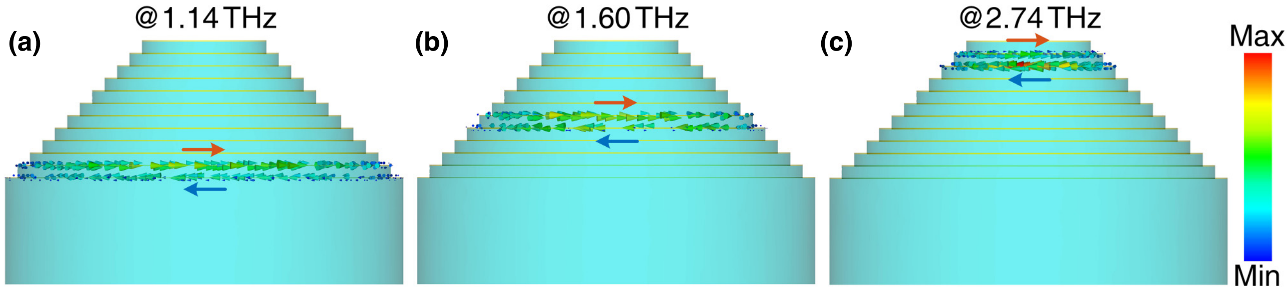

FIG. 10 Surface-current distributions of ultrabroadband THz absorber at various resonant frequencies.

absorption bandwidth of ultrabroadband absorber can be flexibly tuned by adjusting the geometric parameters.

APPENDIX D: SURFACE-CURRENT DISTRIBUTIONS OF THE ULTRABROADBAND THZ ABSORBER

Figures 10(a)–10(c) depicts that the surface-current distributions of proposed ultrabroadband THz absorber at various resonant frequencies, it is clear that the neighboring concentric ring resonators display antiparallel surface-current distributions and thus induce a magnetic resonance, and eventually the overlapping of multiple magnetic resonances at different-level will generate an ultrabroadband absorption spectrum.

APPENDIX E: EFFICIENT CIRCUIT MODEL FOR NARROWBAND METAMATERIAL ABSORBER

In Fig. 11, serially connected R_i, L_i, and C_i represent the equivalent resistance, inductance, and capacitance, respectively, where the subscript, $i = 1, 2$, represents meta-atoms I and II, respectively. The out-of-plane resin substrate is equivalent to the transmission line with a characteristic impedance of Z_r. According to efficient circuit theory, the reflection coefficient (Γ) under normal incidence can be expressed as

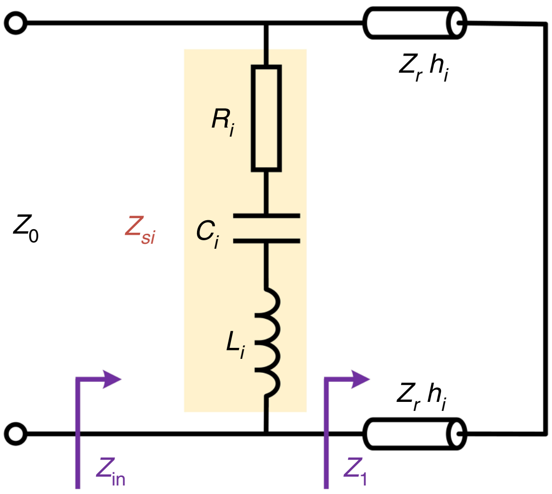

FIG. 11 Efficient circuit model of THz narrowband absorbers.

$$\Gamma = \frac{Z_{\text{in}} - Z_0}{Z_{\text{in}} + Z_0}, \tag{E1}$$

$$Z_{\text{in}} = Z_{si} Z_1 / (Z_{si} + Z_1),\ i = 1,\ 2 \tag{E2}$$

$$Z_1 = j Z_r \tan(k_r h_i),\ i = 1, 2, \tag{E3}$$

$$Z_d = Z_0/\sqrt{\varepsilon_r}, \tag{E4}$$

where Z_0 and Z_r are characteristic impedances of free space and the resin substrate, respectively; $k_r = \omega\sqrt{\varepsilon_0 \varepsilon_r \mu_0}$ is the propagation constant in the resin substrate; ε_0 and μ_0 are the permittivity and permeability of free space, respectively; ε_r is the permittivity of the resin substrate; h_i ($i = 1,\ 2$) is the thickness of the resin substrate; and Z_s are the equivalent impedances of the meta-atoms, which can be expressed as

$$Z_{si} = R_i - j\left(\frac{1 - \omega^2 L_i C_i}{\omega C_i}\right),\ i = 1, 2, \tag{E5}$$

where the efficient resistance, R_i, can be calculated by $R_i = R_s(S/A)$, in which $S = P_i^2$ is the area of the unit cell and A is corrected as the area of the meta-atom region. The equivalent inductances, L_1 and L_2, and capacitances, C_1 and C_2, can be calculated by [33,34]

$$\begin{aligned} L_i &= \frac{X}{Z_0} = R\frac{\pi}{4}\frac{d}{p}\frac{p\cos\theta}{\lambda} \\ &\quad \times \left\{\ln\left[\csc\left(\frac{\pi\omega}{2p}\right) + G(p, \omega, \lambda, \theta)\right]\right\}, \\ C_i &= \frac{B}{Z_0} = R\frac{\pi}{2}\frac{d}{p}\varepsilon_{\text{eff}}\frac{4p\sec\theta}{\lambda} \\ &\quad \times \left\{\ln\left[\csc\left(\frac{\pi g_a}{2p}\right) + G(p, g_a, \lambda, \theta)\right]\right\}, \end{aligned} \tag{E6}$$

where θ is the incident angle; λ and ω are the wavelength and annular frequency of the incident wave, respectively; $g_a = p - \pi d/4$ is the average gap between two adjacent unit cells; p is the period of the unit cell; R is a coefficient that represents the reduction in the reactance or susceptance of the disk compared with those of the concentric ring [34]; and G is a correction term given in Ref. [35].

[1] L. Cong, S. Tan, R. Yahiaoui, F. Yan, W. Zhang, and R. Singh, Experimental demonstration of ultrasensitive sensing with terahertz metamaterial absorbers: A comparison with the metasurfaces, Appl. Phys. Lett. **106**, 031107 (2015).

[2] H. Zhou, X. Hui, D. Li, D. Hu, X. Chen, X. He, L. Gao, H. Huang, C. Lee, and X. Mu, Metal–organic framework-surface-enhanced infrared absorption platform enables simultaneous on-chip sensing of greenhouse gases, Adv. Sci. **7**, 2001173 (2020).

[3] N. Liu, M. Mesch, T. Weiss, M. Hentschel, and H. Giessen, Infrared perfect absorber and its application as plasmonic sensor, Nano Lett. **10**, 2342 (2010).

[4] K. Fan, J. Y. Suen, X. Liu, and W. J. Padilla, All-dielectric metasurface absorbers for uncooled terahertz imaging, Optica **4**, 601 (2017).

[5] C. Zhou, X. Qu, S. Xiao, and M. Fan, Imaging Through a Fano-Resonant Dielectric Metasurface Governed by Quasi–Bound States in the Continuum, Phys. Rev. Appl. **14**, 044009 (2020).

[6] P. Pitchappa, A. Kumar, S. Prakash, H. Jani, R. Medwal, M. Mishra, R. S. Rawat, T. Venkatesan, N. Wang, and R. Singh, Volatile ultrafast switching at multilevel nonvolatile states of phase change material for active flexible terahertz metadevices, Adv. Funct. Mater. **31**, 2100200 (2021).

[7] H. Zhou, C. Yang, D. Hu, D. Li, X. Hui, F. Zhang, M. Chen, and X. Mu, Terahertz biosensing based on bi-layer metamaterial absorbers toward ultra-high sensitivity and simple fabrication, Appl. Phys. Lett. **115**, 143507 (2019).

[8] W. Wang, F. Yan, S. Tan, H. Li, X. Du, L. Zhang, Z. Bai, D. Cheng, H. Zhou, and Y. Hou, Enhancing sensing capacity of terahertz metamaterial absorbers with a surface-relief design, Photonics Res. **8**, 519 (2020).

[9] L. Huang, C.-C. Chang, B. Zeng, J. Nogan, S.-N. Luo, A. J. Taylor, A. K. Azad, and H.-T. Chen, Bilayer metasurfaces for dual- and broadband optical antireflection, ACS Photonics **4**, 2111 (2017).

[10] C.-C. Chang, L. Huang, J. Nogan, and H.-T. Chen, Invited article: Narrowband terahertz bandpass filters employing stacked bilayer metasurface antireflection structures, APL Photonics **3**, 051602 (2018).

[11] S. Savo, D. Shrekenhamer, and W. J. Padilla, Liquid crystal metamaterial absorber spatial light modulator for THz applications, Adv. Opt. Mater. **2**, 275 (2014).

[12] C. C. Chang, Z. Zhao, D. Li, A. J. Taylor, S. Fan, and H. T. Chen, Broadband Linear-to-Circular Polarization Conversion Enabled by Birefringent off-Resonance Reflective Metasurfaces, Phys. Rev. Lett. **123**, 237401 (2019).

[13] P. Nie, D. Zhu, Z. Cui, F. Qu, L. Lin, and Y. Wang, Sensitive detection of chlorpyrifos pesticide using an all-dielectric broadband terahertz metamaterial absorber, Sens. Actuators, B **307**, 127642 (2020).

[14] N. I. Landy, C. M. Bingham, T. Tyler, N. Jokerst, D. R. Smith, and W. J. Padilla, Design, theory, and measurement of a polarization-insensitive absorber for terahertz imaging, Phys. Rev. B **79**, 98 (2009).

[15] X. Zhao, Y. Wang, J. Schalch, G. Duan, K. Cremin, J. Zhang, C. Chen, R. D. Averitt, and X. Zhang, Optically modulated ultra-broadband All-silicon metamaterial terahertz absorbers, ACS Photonics **6**, 830 (2019).

[16] R. H. Fan, B. Xiong, R. W. Peng, and M. Wang, Constructing metastructures with broadband electromagnetic functionality, Adv. Mater. **32**, 1904646 (2019).

[17] D. Xiao, M. Zhu, L. Sun, C. Zhao, Y. Wang, E. H. Tong Teo, F. Hu, and L. Tu, Flexible ultra-wideband terahertz absorber based on vertically aligned carbon nanotubes, ACS Appl. Mater. Interfaces **11**, 43671 (2019).

[18] P. C. Wu, N. Papasimakis, and D. P. Tsai, Self-Affine Graphene Metasurfaces for Tunable Broadband Absorption, Phys. Rev. Appl. **6**, 044019 (2016).

[19] P. Yu, L. V. Besteiro, Y. Huang, J. Wu, L. Fu, H. H. Tan, C. Jagadish, G. P. Wiederrecht, A. O. Govorov, and Z. Wang, Broadband metamaterial absorbers, Adv. Opt. Mater. **7**, 1800995 (2018).

[20] W. Ma, Y. Wen, and X. Yu, Broadband metamaterial absorber at mid-infrared using multiplexed cross resonators, Opt. Express **21**, 30724 (2013).

[21] W. Guo, Y. Liu, and T. Han, Ultra-broadband infrared metasurface absorber, Opt. Express **24**, 20586 (2016).

[22] M. Kenney, J. Grant, Y. D. Shah, I. Escorcia-Carranza, M. Humphreys, and D. R. S. Cumming, Octave-spanning broadband absorption of terahertz light using metasurface fractal-cross absorbers, ACS Photonics **4**, 2604 (2017).

[23] Y. Cui, K. H. Fung, J. Xu, H. Ma, Y. Jin, S. He, and N. X. Fang, Ultrabroadband light absorption by a sawtooth anisotropic metamaterial slab, Nano Lett. **12**, 1443 (2012).

[24] F. Ding, Y. Jin, B. Li, H. Cheng, L. Mo, and S. He, Ultrabroadband strong light absorption based on thin multilayered metamaterials, Laser Photonics Rev. **8**, 946 (2014).

[25] S. Hu, S. Yang, Z. Liu, B. Quan, J. Li, and C. Gu, Broadband and polarization-insensitive absorption based on a set of multisized fabry–perot-like resonators, J. Phys. Chem. C **123**, 13856 (2019).

[26] M. Zhang, F. Zhang, Y. Ou, J. Cai, and H. Yu, Broadband terahertz absorber based on dispersion-engineered catenary coupling in dual metasurface, Nanophotonics **8**, 117 (2018).

[27] C. Du, D. Zhou, H.-H. Guo, Y.-Q. Pang, H.-Y. Shi, W.-F. Liu, J.-Z. Su, C. Singh, S. Trukhanov, A. Trukhanov, L. Panina, and Z. Xu, An ultra-broadband terahertz metamaterial coherent absorber using multilayer electric ring resonator structures based on anti-reflection coating, Nanoscale **12**, 9769 (2020).

[28] X. Cheng, R. Huang, J. Xu, and X. Xu, Broadband terahertz near-perfect absorbers, ACS Appl. Mater. Interfaces **12**, 33352 (2020).

[29] S. Liu, H. Chen, and T. J. Cui, A broadband terahertz absorber using multi-layer stacked bars, Appl. Phys. Lett. **106**, 151601 (2015).

[30] D. Jia, J. Xu, and X. Yu, Ultra-broadband terahertz absorption using bi-metasurfaces based multiplexed resonances, Opt. Express **26**, 26227 (2018).

[31] Z. Du, J. Liang, T. Cai, X. Wang, Q. Zhang, T. Deng, B. Wu, R. Mao, and D. Wang, Ultra-light planar meta-absorber with wideband and full-polarization properties, Opt. Express **29**, 6434 (2021).

[32] J. Zhu, Z. Ma, W. Sun, F. Ding, Q. He, L. Zhou, and Y. Ma, Ultra-broadband terahertz metamaterial absorber, Appl. Phys. Lett. **105**, 021102 (2014).

[33] A. Ramezani Varkani, Z. Hossein Firouzeh, and A. Zeidaabadi Nezhad, Equivalent circuit model for array of circular loop FSS structures at oblique angles of incidence, IET Microw. Antennas Propag. **12**, 749 (2018).

[34] A. R. Varkani, Z. H. Firouzeh, and A. Z. Nezhad, Design of a randomised arrangement AMC surfaces for RCS reduction based on equivalent circuit modelling, IET Microw. Antennas Propag. **12**, 1684 (2018).

[35] R. J. Langley and E. A. Parker, Equivalent circuit model for arrays of square loops, Electron. Lett. **18**, 294 (1982).